Fast beam studies of NCO free radical photodissociation

D. R. Cyr,[a] R. E. Continetti,[b] R. B. Metz,[c] D. L. Osborn,[d] and D. M. Neumark[e]
Department of Chemistry, University of California, Berkeley, California 94720 and Chemical Sciences Division, Lawrence Berkeley Laboratory, Berkeley, California 94720

The spectroscopy and dissociation dynamics of the NCO radical have been investigated by applying fast radical beam photodissociation spectroscopy to the $\tilde{B}\,^2\Pi \leftarrow \tilde{X}\,^2\Pi$ electronic transition. Measurements of the photodissociation cross section as a function of dissociation wavelength show that even the lowest vibrational levels of the $\tilde{B}\,^2\Pi$ state predissociate. Analysis of fragment kinetic energy release reveals that the spin-forbidden $N(^4S) + CO(^1\Sigma^+)$ products are produced exclusively until 20.3 kcal/mol above the origin, at which point, the spin-allowed $N(^2D) + CO$ product channel becomes energetically accessible. The spin-allowed channel dominates above this threshold. By determining the location of this threshold, we obtain a new ΔH^0_f for NCO of 30.5 ± 1 kcal/mol, several kcal/mol lower than the previously accepted value.

I. INTRODUCTION

During the past ten to 15 years, a wide variety of state-selected methods have been developed to study the photodissociation of stable, closed-shell molecules.[1] Ideally, these experiments enable one to map out the dissociative electronic states in the molecule, find the energy needed to break the dissociating chemical bond, and determine in detail the interactions between the departing photofragments. It is clearly of interest to extend the methods of photodissociation to the study of reactive open-shell radicals. At present, however, even the bond dissociation energies, let alone the detailed interactions among the excited electronic states, are poorly characterized in many of these species. Thus far, successful photodissociation experiments have been performed on only a handful of reactive free radicals,[2-4] largely because of the experimental difficulties involved in preparing these species free of contaminants and in reasonably well-defined quantum states. Recently, we have demonstrated that these problems can be overcome by preparing the radical of interest via photodetachment of a mass-selected negative ion beam.[5] This paper describes the application of this method to the photodissociation of the NCO radical.

The NCO radical has attracted considerable interest over the years, both for its role in combustion chemistry and because of its spectroscopic complexity. NCO is believed to be an intermediate in the combustion of nitrogen-containing compounds.[6] It has been observed in CH_4/N_2O flames[7] and is known to be the primary product of the $CN + O_2$ reaction.[8] The spectroscopy of the ground and excited states of NCO is also of interest. The electronic transitions from the ground $\tilde{X}\,^2\Pi$ state to the low-lying $\tilde{A}\,^2\Sigma^+$ and $\tilde{B}\,^2\Pi$ excited states were first observed in 1958[9]

and analyzed in detail by Dixon[10,11] in 1960; the $\tilde{A}\,^2\Sigma^+ \leftarrow \tilde{X}\,^2\Pi$ and $\tilde{B}\,^2\Pi \leftarrow \tilde{X}\,^2\Pi$ origins are at 440 and 315 nm, respectively. Dixon's work on the $\tilde{A}\,^2\Sigma^+ \leftarrow \tilde{X}\,^2\Pi$ system was followed by several optical absorption[12,13] and laser-induced fluorescence[7(a),7(c),14-17] studies. The electronic ground state has been investigated using infrared,[12] electron paramagnetic resonance,[18] microwave,[19] and far infrared laser magnetic resonance[20] spectroscopy. The detailed characterization of the NCO ground state and the $\tilde{A}\,^2\Sigma^+ \leftarrow \tilde{X}\,^2\Pi$ transition has in turn led to a better understanding of the $CN + O_2$ reaction; several groups have measured vibrational, rotational, and fine structure distributions of NCO produced by this reaction using laser-induced fluorescence of the $\tilde{A}\,^2\Sigma^+ \leftarrow \tilde{X}\,^2\Pi$ transition.[21]

The results presented in this paper provide new insight into the $\tilde{B}\,^2\Pi \leftarrow \tilde{X}\,^2\Pi$ system of NCO which, in contrast to the $\tilde{A}\,^2\Sigma^+ \leftarrow \tilde{X}\,^2\Pi$ system, remains largely unassigned. This is due to Renner–Teller and Fermi resonance interactions within the $\tilde{B}\,^2\Pi$ state, as well as extensive perturbations of this state by the nearby lower-lying $\tilde{A}\,^2\Sigma^+$ state and predissociation to N + CO. In fact, one of the key unresolved issues with respect to the $\tilde{B}\,^2\Pi$ state, and certainly the one which motivated the current study, is the identification of the onset of predissociation from the $\tilde{B}\,^2\Pi$ state and the characterization of the dissociation products. Dixon[11] originally observed spectral broadening beginning at the transition to the $v_1 = 2$, $v_2 = 0$, $v_3 = 0$, or (200) level at 33 700 cm^{-1}. This broadening was attributed to predissociation resulting in the spin-allowed $N(^2D) + CO$ products, thereby giving an upper bound of 40 kcal/mol for $D_0(N-CO)$, the bond dissociation energy of NCO to form ground state (but spin-forbidden) $N(^4S) + CO$ products. The corresponding heat of formation is $\Delta H^0_f(NCO) = 45$ kcal/mol. $[D_0(N-CO) = 85.3$ kcal/mol$- \Delta H^0_f(NCO)$ (see the Discussion section).] In a subsequent vacuum ultraviolet photolysis study of HNCO in which the threshold for production of the NCO $\tilde{A}\,^2\Sigma^+$ state was measured, Okabe[22] determined $\Delta H^0_f(NCO)$ to be 37 kcal/mol. This implies that predissociation to $N(^2D) + CO$ can occur only above the (400) level of the $\tilde{B}\,^2\Pi$ state. Okabe's value for $\Delta H^0_f(NCO)$ is consistent with that obtained by Coombe[2]

[a] NSERC (Canada) 1967, Predoctoral Fellow.
[b] Department of Chemistry, University of California, San Diego, La Jolla, California 92093.
[c] Current address: Department of Chemistry, University of Wisconsin-Madison, Madison, WI 53706.
[d] NDSEG Predoctoral Fellow.
[e] NSF Presidential Young Investigator and Camille and Henry Dreyfus Teacher–Scholar.

in a recent study of NCO photodissociation at 193 nm. Crosley[23] found that the fluorescence lifetime of the $\tilde{B}\,^2\Pi$ state was dramatically shorter for the (100) vibrational level ($\leqslant$10 ns) than for the (000) level (63 ns). This was interpreted to mean that the spin-allowed $N(^2D) + CO$ threshold occurs between the (000) and (100) levels of the $\tilde{B}\,^2\Pi$ state, yielding $D_0(N-CO) \leqslant 39$ kcal/mol and $\Delta H_f^0(NCO) \geqslant 48$ kcal/mol.

The observation that the $CN + O_2 \rightarrow NCO + O$ reaction occurs with no appreciable activation barrier[24] means that $\Delta H_f^0(NCO) \leqslant 44$ kcal/mol, and this, in conjunction with the considerable NCO bending excitation produced by the $CN + O_2$ reaction[21(b),21(c)] lends support to Okabe's value for $\Delta H_f^0(NCO)$. However, the extraction of $\Delta H_f^0(NCO)$ from his measurement uses the heat of formation of HNCO, and this in turn requires an accurate value for $\Delta H_f^0(NH)$, for which the spread in recently reported values is several kcal/mol. The most recent determination of $\Delta H_f^0(HNCO)$ by Chandler,[25] when combined with Okabe's work, yields a revised value of 36.1 kcal/mol for $\Delta H_f^0(NCO)$; this is the currently accepted literature value.[26] However, an independent determination of $\Delta H_f^0(NCO)$ from a direct measurement of the N–CO bond dissociation energy is desirable; an accurate value is vital in modeling reaction schemes involving the NCO radical. In addition, one would like to understand the origin of the widely disparate values discussed above.

The NCO photodissociation study reported here addresses all of these issues. We have investigated the $\tilde{B}\,^2\Pi \leftarrow \tilde{X}\,^2\Pi$ electronic transition between 316 and 234 nm. The salient results are as follows: We show unambiguously that all of the vibrational levels of the NCO $\tilde{B}\,^2\Pi$ state dissociate. In addition, translational energy measurements on the photofragments show that the spin-allowed $N(^2D) + CO$ channel is accessible only for vibrational levels higher than the (600) level in the $\tilde{B}\,^2\Pi$ state (greater than 20.3 kcal/mol above the electronic origin), while the lower vibrational levels undergo predissociation to the spin-forbidden $N(^4S) + CO$ channel. We believe that it is this spin-forbidden dissociation which led to the high values of $\Delta H_f^0(NCO)$ inferred by Dixon[11] and Crosley.[23] Finally, our photofragment kinetic energy release measurements near the $N(^2D) + CO$ threshold yield a value of 30.5 $\pm$ 1 kcal/mol for $\Delta H_f^0(NCO)$.

II. EXPERIMENT

Our experiments are based on the idea that since free radicals typically have positive electron affinities, one can generate a very clean source of radicals by laser photodetachment of a mass-selected beam of the precursor negative ion. The resulting radical beam is then dissociated with a second laser. Since the initial kinetic energy of the ion beam is 8 keV, the fragments resulting from photodissociation of the radical have high kinetic energies in the laboratory frame of reference and can be detected directly with high ($\sim$50%) efficiency using a microchannel plate detector. The overall experiment in the case of NCO photodissociation is
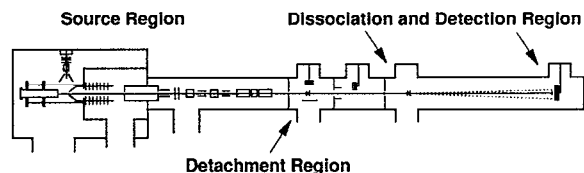
FIG. 1. A schematic illustration of the experimental apparatus. A more detailed diagram and explanation can be found in Ref. 5.

$$NCO^- \underset{h\nu_1}{\rightarrow} NCO(+e^-) \underset{h\nu_2}{\rightarrow} N + CO.$$
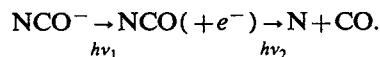
The higher energy $O + CN$ channel is not accessible at the dissociation wavelengths used in this study.

Two types of experiments can be performed. In photodissociation cross section measurements, we determine the total photofragment signal as a function of $h\nu_2$ and thereby map out the dissociative electronic transitions of the NCO radical. In the case of the $\tilde{B}\,^2\Pi \leftarrow \tilde{X}\,^2\Pi$ transition in NCO, one expects a highly structured spectrum since the $\tilde{B}\,^2\Pi$ state undergoes predissociation rather than direct dissociation. Alternatively, at fixed $h\nu_2$, we can measure the photofragment time-of-flight (TOF) distribution at the detector and determine the maximum kinetic energy release and (more approximately) the translational energy distribution of the fragments.

The fast radical beam photodissociation spectrometer use in this work is shown in Fig. 1. The operation of this instrument has been described in detail previously;[5] consequently, only its most important features will be discussed here.

Negative ions are generated using the pulsed molecular beam/electron gun source developed by Lineberger and co-workers[27] and used in several of our other investigations.[28] To make NCO^-, neon (10 psig) is bubbled through benzyl isocyanate (Pfaltz & Bauer) at room temperature and the resulting gas mixture is expanded through a piezoelectric pulsed molecular beam value[29] operating at a 50 Hz repetition rate. A 1 keV electron beam intersects the free jet expansion downstream of the valve orifice, forming NCO^- by dissociative attachment of an electron to the benzyl isocyanate. (A similar scheme was first used by Illenberger et al. to generate N_3^- from benzyl azide.[30]) Since the anions are formed in the continuum flow region of the free jet expansion, they experience significant vibrational and rotational cooling.

The ions pass through a skimmer and are accelerated to 8 keV. They then pass through a pulsed high voltage switch[31] which enables us to run an 8 keV ion beam through the instrument while maintaining the source and detector regions at ground potential. The ions are then mass selected using a coaxial, beam-modulation TOF mass spectrometer;[32] this design induces a negligible kinetic energy spread in the ion beam, an important and desirable feature for the photofragment TOF measurements described below.

The ion beam passes through a 1 mm diameter aperture into the photodetachment region. Here, the ions are

crossed by an excimer-pumped dye laser beam (Lambda Physik LPX 210i and FL3002, PTP dye from Exciton) timed to intercept only the ion mass of interest and operating at 339 nm (nearly the peak of the PTP dye curve). The photodetachment wavelength is chosen to allow production of only the ground vibrational state of the neutral free radical. The photoelectron spectrum[33] of NCO$^-$ indicates that at 339 nm, no excited vibrational states of the neutral free radical will be formed from the ground vibrational state of the ion, so the vibrational distribution attained during the supersonic expansion is preserved. Photodetached electrons are collected and detected using a microchannel plate (MCP) detector; the resulting signal is stored for subsequent normalization of the photodissociation spectrum. Any undetached anions are deflected out of the beam, leaving a mass-selected, fast beam of neutral free radicals. These pass through another 1 mm collimating aperture and enter the photodissociation and detection region.

In this region, the radicals are crossed with the laser beam from a second excimer-pumped dye laser system, the output of which is doubled using the appropriate doubling crystal. The dyes used to cover the broad range of dissociation wavelengths (from 632 to 468 nm in the fundamental wavelength) were R640, R6G, R610, R590, C540A, C503, and C480 (Exciton). Laser pulse energies were typically 1–2 mJ after doubling and the linewidth of the doubled light was 0.4 cm^{-1}. This is what determines the resolution of our spectra; the Doppler broadening in our experiment is only 0.02 cm^{-1}. Depending on the arrangement of right angle prisms used to direct the laser beam into the spectrometer, the laser polarization direction could be made either parallel or perpendicular to the radical beam axis.

The resulting photofragments are detected by a 40 mm diameter MCP which can be placed either 67.8 or 101.1 cm downstream of the photodissociation region. Any neutrals that strike this detector have sufficient laboratory kinetic energy to be detected with high efficiency. The center of this detector is shielded by a 3.0 mm wide beam block to prevent undissociated NCO radicals from impinging on the detector face. The N+CO fragments typically have enough center-of-mass translational energy to miss the beam block, but not so much energy that they miss the detector entirely.

In the photodissociation cross section measurements, the photofragment yield is determined as a function of the dissociation dye laser wavelength. At each wavelength, the MCP signal is measured with an analog-to-digital converter interfaced to a microcomputer. A step size of 0.02 nm, with 500–1000 shots per point, is typically used to gather a survey scan, which provides sufficient resolution for the observation of rotational contours of NCO bands. Where strong photodissociation signal is observed, scans were taken with a step size of 0.001 nm and a laser pulse energy of 100 μJ to minimize power broadening.

In the photofragment TOF experiments, the photodissociation laser wavelength is fixed, while the photofragment MCP signal is collected and summed over 10 000–40 000 laser shots by a 200 MHz LeCroy transient digitizer
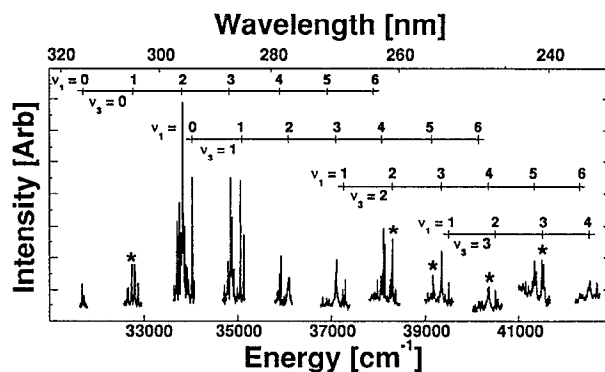
FIG. 2. A compilation of survey scans (0.02 nm step size) of the NCO $\tilde{B}\,^2\Pi \leftarrow \tilde{X}\,^2\Pi$ photodissociation cross section. Progressions in the ν_1 vibration and the ν_3 vibration are indicated. The spectrum shows that the (000) level of the $\tilde{B}\,^2\Pi$ state predissociates. Asterisks (*) illustrate dissociation wavelengths where TOF data presented below were obtained.

interfaced to a microcomputer. TOF spectra were taken with both parallel and perpendicular laser polarization orientations at several wavelengths in order to determine the photofragment energy and angular distribution. For comparison, TOF spectra of the undissociated parent radical were obtained by blocking the dissociation laser and translating the MCP detector so that the radical beam missed the beam block and hit the detector.

III. RESULTS

Figure 2 shows the compilation of our photodissociation cross section measurements (0.02 nm step size) on the $\tilde{B}\,^2\Pi \leftarrow \tilde{X}\,^2\Pi$ system over a total range of 82 nm, from 316 to 234 nm. These measurements cover a wider wavelength range than Dixon's original work[11] and are at higher resolution than the matrix isolation spectra of Milligan and Jacox.[12] Preliminary scans, at a lower resolution than Fig. 2, across the entire wavelength range enabled us to concentrate further scans in the regions where the predissociation signal was observed. Therefore, the apparent gaps in our survey spectrum are regions that were found not to contain peaks of significant intensity. The intensity of the signal presented here is not normalized to laser power, since at the laser fluence customarily used for these survey scans (100–200 mJ/cm^2), the transitions could have been saturated.

To the extent that the spectrum in Fig. 2 can be assigned, it appears to consist of progressions in the ν_1 and ν_3 vibrational modes of the $\tilde{B}\,^2\Pi$ state with fundamental frequencies of approximately 1047 and 2303 cm^{-1}, respectively. (These values were obtained in Dixon's study.[11]) The assignments for the location of the various ($\nu_1 0\nu_3$) vibrational levels of the $\tilde{B}\,^2\Pi$ state are indicated in Fig. 2. An enlargement of the spectral region in Fig. 2 containing the (100)–(000) band is shown in Fig. 3. Figure 4 shows a higher resolution scan (laser step size=0.001 nm) of the subbands labeled (d) and (e) in Fig. 3; the more intense subband (d) is the main $^2\Pi_{3/2}$–$^2\Pi_{3/2}$ transition, which was one of the two subbands analyzed by Dixon in his original
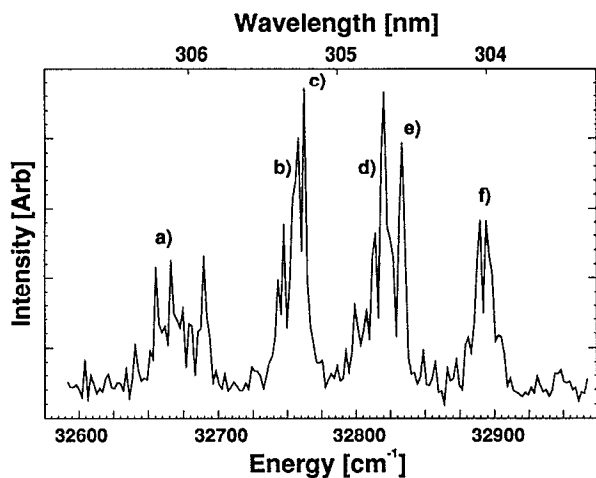
FIG. 3. A survey scan in the region of the $\tilde{B}\,^2\Pi(100) \leftarrow \tilde{X}\,^2\Pi(000)$ band. Labels (a)–(f) indicate individual subbands; (b) and (d) are the previously assigned (Ref. 11) $^2\Pi_{1/2}-\,^2\Pi_{1/2}$ and $^2\Pi_{3/2}-\,^2\Pi_{3/2}$ subbands, while the other peaks have been tentatively assigned here as $(020) \leftarrow (000)$ subbands: (a) $\mu-^2\Pi_{1/2}-\,^2\Pi_{1/2}$; (c) $\mu-\,^2\Pi_{3/2}-\,^2\Pi_{3/2}$; (e) $\kappa-\,^2\Pi_{1/2}-\,^2\Pi_{1/2}$; and (f) $\kappa-\,^2\Pi_{3/2}-\,^2\Pi_{3/2}$. These transitions are shown schematically in Fig. 7.

work on this system. Linewidths in Fig. 4 are instrument limited to $\cong 0.4$ cm^{-1} full width at half-maximum (FWHM) corresponding to the laser resolution.

Since we observe a signal *only when NCO dissociates* during the flight time between the photodissociation volume and the photofragment detector (about 5.27 μs for a 101.1 cm flight length), the spectrum in Fig. 2 shows that the $\tilde{B}\,^2\Pi$ state predissociates over the entire $\tilde{B}\,^2\Pi \leftarrow \tilde{X}\,^2\Pi$ system. Predissociation is observed even from the $\tilde{B}$ state (000) level, although the intensity of the photofragment signal was considerably less than for the bands further to the blue. This differs from the $\tilde{B}\,^2\Pi \leftarrow \tilde{X}\,^2\Pi$ absorption spectrum, in which transitions to the (000) level appear to
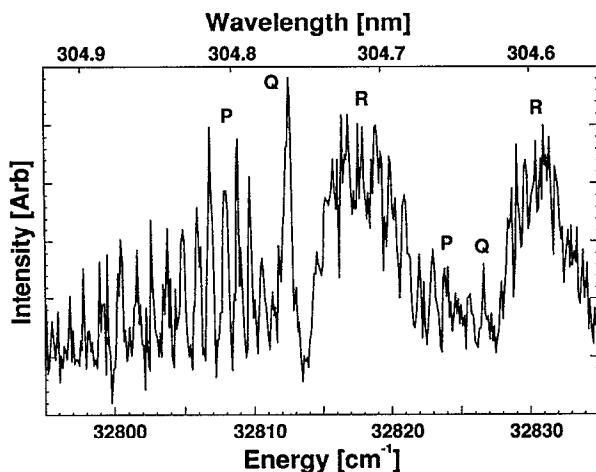
FIG. 4. A finer scan (0.001 nm step size) of subbands (d) and (e) in Fig. 3. See Fig. 7 for assignments. The *P*, *Q*, and *R* branches in the two subbands are labeled.
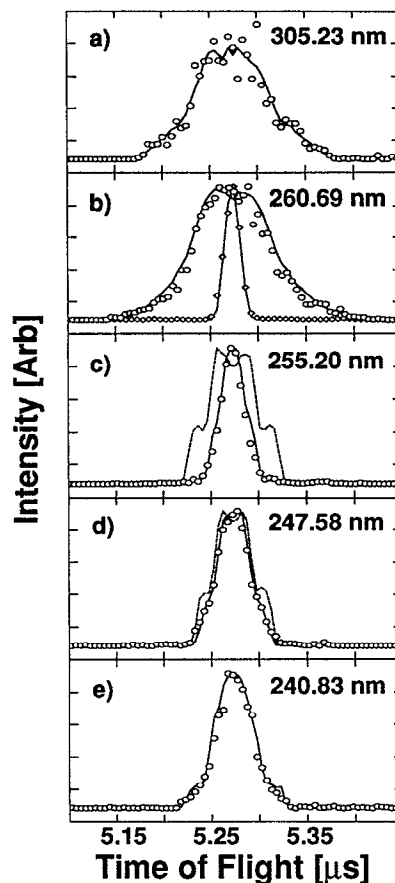
FIG. 5. TOF data (circles) obtained with a flight length of 101.1 cm at five photodissociation wavelengths as indicated. Various simulations (solid and dashed lines) are discussed in the text.

be at least as intense as the transitions to higher levels. The implications of these observations for the NCO dissociation dynamics and energetics are discussed below.

Photofragment TOF spectra were taken at dissociation wavelengths of 305.23, 260.69, 255.20, 247.58, and 240.83 nm (vacuum corrected) with the detector 101.1 cm from the photodissociation volume and the laser polarization such that the *E* vector was parallel to the direction of the radical beam propagation. These wavelengths correspond to the peaks marked with an asterisk in Fig. 2. The five experimental spectra are displayed in Fig. 5. The narrow peak shown in Fig. 5(b) is a typical undissociated radical beam TOF profile, which was obtained to allow evaluation of the energy spread in the undissociated radical beam for incorporation into simulations of the dissociation spectra. In addition, TOF spectra at 260.69, 255.20, and 247.58 nm were taken with the detector 67.8 cm from the photodissociation volume with the laser polarization parallel and perpendicular to the radical beam axis. These are shown in Fig. 6. The spectra obtained with the two orthogonal laser polarizations are very similar, implying a nearly isotropic photofragment angular distribution. The most striking result seen in both figures is the abrupt narrowing of the TOF distribution between 260.69 and 255.20 nm, which

Parallel   Perpendicular
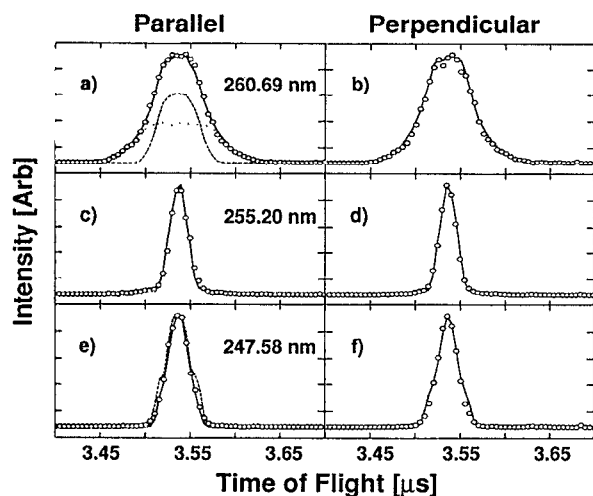
FIG. 6. TOF data (circles) obtained with a flight length of 67.8 cm at three wavelengths with the dissociation laser output polarized both parallel and perpendicular to the ion beam axis as indicated. Various simulations (solid and dashed lines) are discussed in the text.

suggests that a new dissociation channel opens in that wavelength interval.

IV. ANALYSIS

A. NCO spectroscopy

The $\tilde{B}\,^2\Pi \leftarrow \tilde{X}\,^2\Pi$ system in NCO has proved notoriously difficult to assign. The $\tilde{X}\,^2\Pi$ state vibrational energy level structure is complicated by Renner–Teller coupling and Fermi resonances between the ν_1 and ν_2 modes. These effects are also expected in the $\tilde{B}\,^2\Pi$ state along with perturbations from the $\tilde{A}\,^2\Sigma^+$ state. In Dixon's original spectrum,[11] only the $(100) \leftarrow (000)$ band had enough extended rotational structure and was sufficiently unperturbed to permit any rotational analysis; this led to an identification of the main $^2\Pi_{1/2}{-}^2\Pi_{1/2}$ and $^2\Pi_{3/2}{-}^2\Pi_{3/2}$ subbands. A rotational analysis of the $(000) \leftarrow (000)$ band was obtained only recently in a double resonance experiment.[34] Dixon found that the bands to the blue of the $(100) \leftarrow (000)$ band were broadened, presumably by predissociation, preventing any rotational analysis. Although these higher energy bands can be tentatively assigned to progressions in the ν_1 and ν_3 modes of the $\tilde{B}\,^2\Pi$ state, the detailed vibrational structure within each band seen in Fig. 2 and in Ref. 11 remains largely unexplained. In this section, we consider what additional information can be gleaned about the spectroscopy of the $\tilde{B}\,^2\Pi \leftarrow \tilde{X}\,^2\Pi$ transition from our photodissociation cross section measurements.

The rotationally resolved spectrum in Fig. 4 is a section of the $(100) \leftarrow (000)$ band. The main P, Q, and R branches noted are from the previously assigned $^2\Pi_{3/2}{-}^2\Pi_{3/2}$ subband. A second, less intense transition is also shown just to the blue of this main subband, and the P branch associated with this transition extends into the R branch head of the main subband. In comparison to Dixon's spectrum, the intensity distribution of the more in-

tense band in Fig. 4 reflects a substantially lower rotational temperature for the NCO radicals. The R and P branches in Fig. 4 fall off in intensity at considerably lower J values. In addition, we observe a strong Q branch, while none was seen in his spectrum; in a $\Pi \leftarrow \Pi$ transition, the intensity of the Q branch falls off rapidly with increasing J. The lower rotational temperature in our experiment is not too surprising because our radicals are generated by photodetachment of a jet-cooled anion beam as opposed to flash photolysis. Simulations of our spectrum indicate a rotational temperature of about 50 K.

In the absence of perturbations or sequence bands, the $(100) \leftarrow (000)$ band should consist of only two subbands (the aforementioned $^2\Pi_{1/2}{-}^2\Pi_{1/2}$ and $^2\Pi_{3/2}{-}^2\Pi_{3/2}$ transitions) whose origins are separated approximately by $|A''-A'| = 18.9$ cm^{-1}, where $A'' = -95.5$ cm^{-1} and $A' = -76.6$ cm^{-1} are the spin–orbit coupling constants in the $\tilde{X}\,^2\Pi$ and $\tilde{B}\,^2\Pi$ states of NCO, respectively.[13,34] Instead, Fig. 3 shows four well-separated subbands labeled (a), (b), (d), and (f) with approximate origins at 32 665, 32 750, 32 814, and 32 890 cm^{-1}, respectively. In addition, as mentioned above, there is an additional subband just to the blue of the main $^2\Pi_{3/2}{-}^2\Pi_{3/2}$ band at 32 829 cm^{-1} [labeled (e)], and a higher resolution scan of the main $^2\Pi_{1/2}{-}^2\Pi_{1/2}$ subband shows a similar subband at 32 760 cm^{-1} [labeled (c) in Fig. 3]. Thus, the $(100) \leftarrow (000)$ band consists of at least six subbands; only two of these have been assigned—(b) to the main $^2\Pi_{3/2}{-}^2\Pi_{3/2}$ subband and (d) to the $^2\Pi_{1/2}{-}^2\Pi_{1/2}$ subband. However, the splitting between the origins of subbands (b) and (d) is 64 cm^{-1}, rather than 19 cm^{-1} as expected from the difference of spin–orbit coupling constants. Thus, even this relatively well-understood band in the $\tilde{B}\,^2\Pi \leftarrow \tilde{X}\,^2\Pi$ transition is quite complex and we wish to consider possible explanations for its appearance.

Previous studies of the electronic spectroscopy of BO$_2$ and CO$_2^+$ provide a wealth of information which can be used to interpret the spectrum of the isoelectronic NCO radical. The $\tilde{A}\,^2\Pi_u \leftarrow \tilde{X}\,^2\Pi_g$ absorption system in BO$_2$ was first seen at high resolution by Johns,[35] while the emission spectroscopy of the $\tilde{A}\,^2\Pi_u \rightarrow \tilde{X}\,^2\Pi_g$ system in CO$_2^+$ has been studied extensively by Rostas and co-workers.[36] Both the (100)–(000) band in BO$_2$ and the (000)–(100) band in CO$_2^+$ exhibit several vibrational features in addition to the two expected subbands. In both cases, there are subbands due to Fermi resonances between the (100) and (020) levels present; $\nu_1 \approx 2\nu_2$ in the $\tilde{A}\,^2\Pi$ state of BO$_2$ and the $\tilde{X}\,^2\Pi$ state of CO$_2^+$. The (020) levels are further split by the combination of Renner–Teller and spin–orbit interactions. The theoretical treatment for this combination of effects has been worked out in a series of papers by Pople[37] and Hougen.[38]

While a (000)–(020) band in a transition between two $^2\Pi$ electronic states is normally very weak, the (020) levels of Π vibronic symmetry borrow intensity from the nearby (100) levels (which also have Π vibronic symmetry). As discussed by Johns[35] and Larcher *et al.*,[36(b)] this interaction leads to as many as six subbands in what is nominally a (100)–(000) band, since the μ and κ $^2\Pi_P$ ($P=1/2,3/2$,
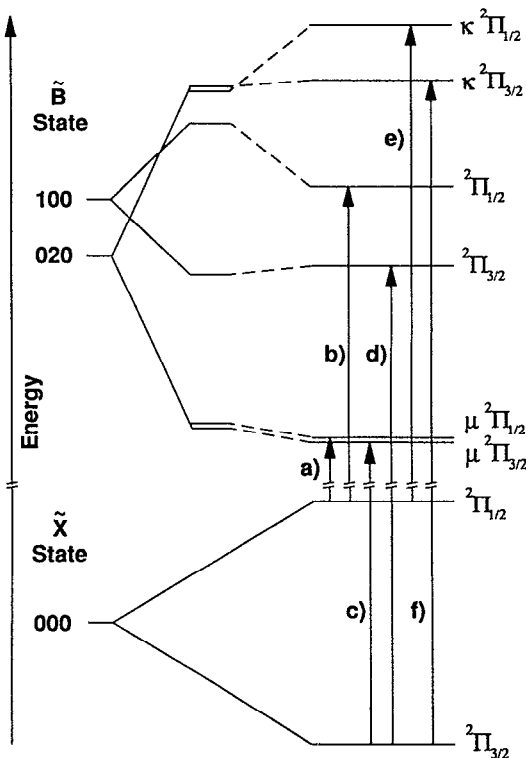
FIG. 7. A schematic showing our tentative assignment of the subbands observed in the (100) ← (000) transition region. The observed transitions yield the following spacings for the 100 and 020 energy levels in the $\tilde{B}\,^2\Pi$ electronic state, relative to the lowest $\mu-^2\Pi_{3/2}$ level: $\mu-^2\Pi_{1/2}$ (0.6 cm^{-1}); $^2\Pi_{3/2}$ (54 cm^{-1}); $^2\Pi_{1/2}$ (85 cm^{-1}); $\kappa-^2\Pi_{3/2}$ (130 cm^{-1}); $\kappa-^2\Pi_{1/2}$ (164.6 cm^{-1}).

where $P = |\pm\Omega\pm l|$) states associated with the (020) level each borrow intensity from the $^2\Pi_P$ state associated with the (100) level (see Fig. 7). In addition, because of energy level shifts associated with the Fermi resonance, the splitting between the (100) $^2\Pi_{1/2}$ and $^2\Pi_{3/2}$ levels can be quite different from the value expected based on spin–orbit coupling alone.

In NCO, where $v_1 \approx 2v_2$ in the $\tilde{X}\,^2\Pi$ and $\tilde{A}\,^2\Sigma^+$ electronic states, effects from Fermi resonances have been observed in both states.[14,20(b)] Although v_2 has not been measured for the $\tilde{B}\,^2\Pi$ state, a recent theoretical study by Alexander and Werner[39] predicts harmonic frequencies of 1080 and 522 cm^{-1} for these stretching and bending modes, so one might expect Fermi resonances in this state as well. The observation of at least six subbands in Fig. 3 is consistent with this expectation, as is the deviation of the splitting between bands (b) and (d) from $|A'-A''|$.

Figure 7, adapted from Johns' paper,[35] shows an energy level diagram consistent with the structure in the (100)–(000) band. The (100) and (020) $\tilde{B}$ state levels with Π vibronic symmetry are shown, from left to right, with no interactions, spin–orbit and Renner–Teller coupling, and finally, the additional effect of Fermi resonances. On the left, the unperturbed (100) level lies above the (020) level in accordance with Alexander's calculation. In the middle set of levels, Dixon's value for the $\tilde{B}$ state spin–

orbit coupling constant $(A' = -76.6$ cm$^{-1})$ is used for the (100) and (020) manifolds, along with a Renner–Teller parameter sufficiently large so that the (100) levels lie within the (020) levels with Π symmetry [the two (020) levels with Φ symmetry are not shown]. The rightmost set of levels shows the qualitative effect of the Fermi resonance between the (100) and (020) manifolds. Since nearby levels with the same P value repel one another, the (100) $^2\Pi_{1/2}$ and $^2\Pi_{3/2}$ levels are forced closer together. This results in a splitting between the main $^2\Pi_{1/2}-^2\Pi_{1/2}$ and $^2\Pi_{3/2}-^2\Pi_{3/2}$ transitions which is larger than $|A'-A''|$, as is seen in the experimental spectrum. Carrying this one step further, the six subbands identified in Fig. 3 can be assigned to the transitions labeled in Fig. 7, assuming the energy level spacings indicated in the caption of Fig. 7.

While Fig. 7 offers an explanation for the appearance of the (100)–(000) band, other possible sources for the multiple subbands must also be considered. For example, perturbations from the lower-lying $\tilde{A}\,^2\Sigma^+$ state are prominent in the $\tilde{B}\,^2\Pi$ (000) ← $\tilde{X}\,^2\Pi$ (000) band[34] and may well be contributing to the (100)–(000) band. At higher resolution, subband (a), in particular, appears to actually consist of two distinct features, one centered at 32 665 cm^{-1} (the value used in the above discussion) and the other at 32 689 cm^{-1}, possibly resulting from extensive $\tilde{A}$ state perturbations. Similar perturbations have been identified in a double resonance study of CO_2^+.[40] In addition, the (100)–(000) transition in NCO may be overlapped by sequence bands in the NCO bend [the (110)–(010) band, e.g.]. Any bend excitation in NCO$^-$ is transferred to NCO when the radical is produced by photodetachment because bend sequence bands in the NCO$^-$ photoelectron spectrum fall on top of the NCO(000) ← NCO$^-$(000) transition. We note that bend sequence bands were observed in our photodissociation study of N_3.[5]

With higher resolution data over a wider frequency range than in the rotationally resolved spectrum in Fig. 4, we might be able to definitively sort out these possibilities. As it is, the qualitative similarities with the CO_2^+ and BO_2 spectra support the notion that most of the detailed structure in the (100) ← (000) band in NCO is from Fermi resonances within the $\tilde{B}\,^2\Pi$ state. These effects will become even more complex for higher energy transitions in the $\tilde{B}\,^2\Pi \leftarrow \tilde{X}\,^2\Pi$ system.

B. Dissociation dynamics

In this section, the photofragment time-of-flight (TOF) results are analyzed in order to learn about the dissociation dynamics of the NCO $\tilde{B}\,^2\Pi$ state. This data can be considered at two levels of detail. We obtain the approximate maximum photofragment kinetic energy release at each wavelength from the edges of the TOF distribution. We also obtain more precise and detailed photofragment energy and angular distributions by comparing experimental and simulated TOF spectra at various laser wavelengths and polarizations.

We first consider the five TOF spectra shown in Fig. 5. In the center-of-mass frame of reference, the fastest N atoms scattered parallel and antiparallel to the ion beam

TABLE I. The summary of results obtained directly from TOF spectra shown in Fig. 5. Kinetic energy release (KER) values are determined using Eq. (1) (see the text).

Wavelength (nm)	$h\nu$ (eV)	$\Delta\tau$ (ns)	KER (eV)	$h\nu$–KER (eV)
305.23	4.06	220	1.74	2.32
260.69	4.76	265	2.52	2.24
255.20	4.86	75	0.20	4.66
247.58	5.01	100	0.36	4.65
240.83	5.15	120	0.52	4.63

FIG. 8. Energy level diagram showing the position of the NCO electronic energy levels relative to the asymptotic energies of the fragment channels as determined by this work.

direction correspond to the minimum (τ_{min}) and maximum (τ_{max}) flight times at which photofragment signal is observed. If effects due to the energy spread of the radical beam and the extent of the beam block are ignored (these *are* considered explicitly below), then $\Delta\tau = \tau_{max} - \tau_{min}$ is related to the maximum center-of-mass kinetic energy release (KER) by

$$KER = \frac{v_b^4}{8l^2} \cdot \left(\frac{m_N \cdot m_{NCO}}{m_{CO}}\right) \cdot (\Delta\tau)^2, \qquad (1)$$

where l is the distance the fragments travel to the detector (101.1 cm for these spectra) and v_b is the beam velocity (1.91×10^7 cm/s). The results for the spectra in Fig. 5 are shown in Table I.

The quantity ($h\nu$ – KER) corresponds to the bond dissociation energy if ground state products are formed. Any excitation present in the products reduces the KER and makes this quantity larger. The more detailed simulations discussed below show that the values for the KER in Table I are only approximate upper bounds to the maximum photofragment kinetic energy release. Therefore, the values of ($h\nu$ – KER) are only approximate lower bounds for the bond dissociation energy plus product internal energy.

Nonetheless, several features in this table are noteworthy. First, consider the value for the KER at $\lambda = 305$ nm, which corresponds to excitation of the $(100) \leftarrow (000)$ transition. If the upper state were dissociating to the lowest energy spin-allowed dissociation channel $N(^2D) + CO$, then KER = 1.78 eV yields $\Delta H_f^0(NCO) = 88$ kcal/mol, more than double the accepted value. This value for $\Delta H_f^0(NCO)$ would mean that the $CN + O_2 \rightarrow NCO + O$ reaction is endothermic by 45 kcal/mol, a physically unreasonable result because this reaction is rapid at room temperature. The 305 and 261 nm TOF results therefore indicate that the upper states for both transitions are dissociating to the energetically allowed, but spin-forbidden $N(^4S) + CO$ channel, which lies 2.38 eV (54.9 kcal/mol) below the $N(^2D) + CO$ channel. However, at $\lambda = 255$ nm, the TOF distribution narrows abruptly. This suggests an energy level diagram for NCO and its photofragments as given in Fig. 8; at $\lambda = 255$ nm, the spin-allowed channel $N(^2D) + CO$ channel is energetically accessible, whereas it is not at $\lambda = 261$ nm.

The results in Table I therefore imply that the $N(^2D) + CO$ channel becomes accessible between 4.76 and 4.86 eV above the NCO ground state and allows us to
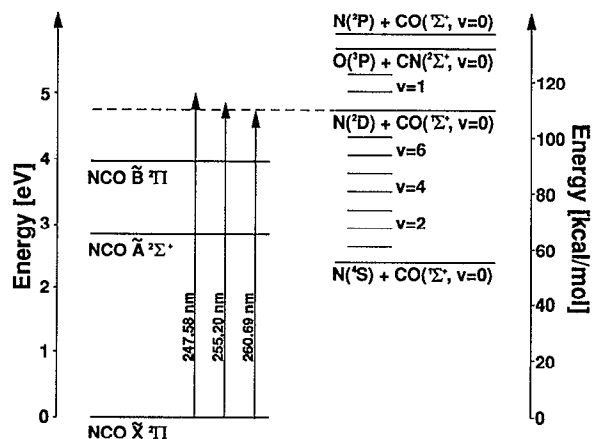
bracket $\Delta H_f^0(NCO)$ between 31.5 and 29.0 kcal/mol. This bracketing is validated by the additional observation that the KER is small at the longest wavelength at which $N(^2D) + CO$ is formed, implying no substantial barrier to dissociation. Since this range of $\Delta H_f^0(NCO)$ values lies below the accepted literature[26] value of 36.1 kcal/mol, we have performed more detailed analyses of photofragment TOF spectra which will now be discussed.

We wish to determine the N–CO bond dissociation energy and the photofragment energy and angular distributions consistent with the TOF spectra in Fig. 5 and 6. This is done using a Monte Carlo computer simulation program,[41] which generates a TOF spectrum for given dissociation wavelength, laser polarization, and radical beam characteristics. The simulation program also accounts for the finite size of the photofragment detector and the beam block. The radical beam characteristics are checked by comparing simulated and experimental TOF spectra of the undissociated radical beam; the agreement, shown in Fig. 5(b), is excellent. The simulation assumes a spread of 8 eV (0.1%) in the ion beam energy. This value is consistent with the small energy spread expected from the beam-modulation TOF mass spectrometer.[42]

To carry out a photofragment TOF simulation, we specify a trial photofragment angular distribution and bond dissociation energy. The simulation program accounts for contributions to the TOF spectra by both N and CO fragments, since the experimental spectrum has contributions from both. Figure 6(a) shows the individual contributions of the N (dotted lines) and CO (dashed lines) fragments as determined from the simulation program together with their sum that fits the experimental TOF spectrum. The fact that only N atoms contribute to the TOF signal close to τ_{min} and τ_{max} is illustrated clearly by this figure.

The photofragment center-of-mass kinetic energy and angular distribution $P(E_T, \theta)$ is taken to be

TABLE II. Simulation parameters used to fit all data in Fig. 6 (both polarizations) and the common wavelengths in Fig. 5. The value shown for D_0(N–CO) was determined by obtaining the best fit for *all* data in both Figs. 5 and 6.

λ (nm)	^4S: ^2D ratio	β (^2D channel)	β (^4S channel)	D_0(N–CO) (kcal/mol)
260.69	100:0	N/A	+0.1	54.9
255.20	6:94	+0.2	+0.1	54.9
247.58	2:98	+0.2	+0.1	54.9

$$P(E_T,\theta) = \sum_{i=S,D} n_i P_i(E_T) * [1 + \beta_i P_2(\cos\theta)]. \quad (2)$$

The index i specifies the N atom electronic state (^4S or ^2D). Here n_i refers to the N atom electronic state populations, $P_i(E_T)$ is the photofragment kinetic energy distribution in the ith electronic state, θ is the angle between the fragment recoil and laser polarization vector, and β_i is the anisotropy parameter[43] for the ith electronic state. $P_i(E_T)$ is determined by specifying the bond dissociation energy and the CO vibration–rotation distribution associated with the ith N atom electronic state.

We first consider the TOF spectra at the three wavelengths for which the photofragment flight length was 67.8 cm (Fig. 6), as these were taken with both laser polarization directions. The broad TOF spectrum at $\lambda = 260$ nm indicates dissociation to N(^4S)+CO, while the two narrower spectra at $\lambda = 255$ and 247 nm are from dissociation primarily to N(^2D)+CO. However, the narrow peak in the 255 nm TOF spectrum sits atop a small, broad pedestal due to a small amount of N(^4S)+CO production. At all three wavelengths, the spectra taken with the laser horizontally polarized (parallel to the radical beam axis) are slightly broader than the spectra taken with vertical laser polarization. This indicates that the anisotropy parameter β is positive for both N atom product electronic states; we find $\beta = +0.1$ for the N(^4S) channel and $\beta = +0.2$ for the N(^2D) channel. The complete set of parameters used to arrive at the solid line fits for the three sets of TOF spectra are listed in Tables II and III.

The narrow peak in the 255 nm TOF spectrum can be fit successfully assuming a single value for the photofragment kinetic energy of 0.10 eV. If this corresponds to the translational energy of N(^2D)+CO($v=0$, $J=0$) fragments, then the N(^2D)+CO dissociation channel lies 4.76 eV (109.8 kcal/mol) above the ground state of NCO, yielding a N–CO bond dissociation energy [to form N(^4S)+CO] of 2.38 eV (54.9 kcal/mol). This value of the bond dissociation energy is the one used to determine the relative energies of NCO and the dissociation product channels in Fig. 8.

Our interpretation of the 255 nm spectrum is supported by simulations of the 247 nm spectrum using the same bond dissociation energy in which the edges of the distribution are fit accurately assuming they are also from N(^2D)+CO($v=0$, $J=0$) fragments. However, closer to the center of the distribution, the simulated TOF spectrum is too broad [Fig. 6(e), dashed line] if *all* the CO is assumed to be in its ($v=0$, $J=0$) state. The best simulation (solid line) includes some rotational excitation in the CO fragment. [CO($v=1$) is not accessible at 247 nm]. The rotational excitation was incorporated using the following empirical functional form for the translational energy distribution:

$$P(E_T) = 1 - \frac{E_T}{E_{TOT}}. \quad (3)$$

Here E_T is translational energy, while E_{TOT} is $h\nu - [D_0(\text{N–CO}) + \Delta E(^2D^{-4}S)]$, where $\Delta E(^2D - {}^4S)$ is the difference in energy between the ^2D and ^4S N atom states.

In the simulated 261 nm TOF spectrum, the photofragment kinetic energy distribution was determined using the bond dissociation energy, determined above, of 2.38 eV. The CO(v, $J=0$) distribution used is given in Table III. A more detailed distribution involving CO vibrational and rotational excitation is not justified by the data. However, one can safely say that unless CO is extremely rotationally excited, the CO vibrational distribution is highly inverted. More significantly, from the perspective of the NCO energetics, τ_{min} and τ_{max} in the simulated TOF distribution, which are due to N(^4S)+CO($v=0$), match the experimental spectrum very well, further supporting the bond dissociation energy obtained from the 255 nm spectrum. As mentioned above, the 255 nm and, to an even lesser extent, the 247 nm spectra have a small contribution from N(^4S)+CO product. The electronic branching ratios in Table II were determined assuming the same CO vibrational distribution for the N(^4S)+CO product that was determined for the 261 nm spectrum.

As a further check on the values determined in these simulations, the parameters in Tables II and III were used to fit the three TOF spectra in Fig. 5 at the same three wavelengths, but where the photofragment flight length is 101.1 cm. Excellent agreement is found between the experimental and simulated TOF spectra. Finally, the TOF spectra in Fig. 5 at both 305 and 240 nm were fit assuming the respective β values obtained above for the two N atom

TABLE III. CO fragment vibrational distribution used in the simulations of the three TOF spectra at 260.69 nm in Figs. 5 and 6. The simulations assumed no rotational excitation of CO.

λ (nm)	$v=0$ population	$v=1$ population	$v=2$ population	$v=3$ population	$v=4$ population	$v=5$ population	$v=6$ population	$v=7$ population	$v=8$ population
260.69	1.0	1.0	1.0	1.0	1.5	2.5	3.0	2.0	1.0

TABLE IV. CO fragment vibrational distribution (neglecting rotational excitation) used in simulation of the TOF spectra in Fig. 5 at 305.23 nm [for N(^4S)+CO products] and 240.83 nm [for N(^2D)+CO products].

λ (nm)	$v=0$ population	$v=1$ population	$v=2$ population	$v=3$ population	$v=4$ population	$v=5$ population
305.23	1.0	1.5	2.5	3.0	3.0	1.0
240.83	1.0	1.0	...	...	...	...

electronic channels. The fragment state populations that gave the best-fitting simulations (solid lines in Fig. 5) are listed in Table IV. The CO vibrational distribution at 305 nm appears to be highly inverted, just as at 260 nm, while the excellent fit at the extrema of the simulation to the data further confirms our choice of D_0(N–CO). At 240 nm, again using D_0(N–CO)=2.38 eV in our simulation, the N(^2D)+CO($v=1$) channel should be energetically accessible. Indeed, the shape of the TOF spectrum is noticeably different from the 247 nm spectrum, with broader wings under a central peak, and we find by varying only the relative vibrational level population of $v=0$ and $v=1$ (neglecting rotational excitation) that an adequate fit is obtained if 50% of the CO is in the $v=1$ level.

The value of 2.38 eV for D_0(N–CO) was obtained from our analysis assuming NCO is in its rotational ground state. Including the correction for the average rotational energy of NCO (0.1 kcal/mol at 50 K), we obtain ΔH_f =30.4 kcal/mol at 0 K. ΔH_f^0(NCO) at 298 K is only slightly higher (30.5 kcal/mol).[44] This value is significantly lower than the currently accepted literature value[26] of 36.1±1 kcal/mol [D_0(N–CO)=2.13 eV]. As a measure of the sensitivity of our TOF spectra to the assumed value of D_0(N–CO), Fig. 5(c) shows the results of a simulation (dotted line) at 255 nm with D_0(N–CO)=2.13 eV, but with all the other parameters the same as in Table II. This is clearly inferior to the simulation with D_0(N–CO)=2.38 eV. Based on trial simulations at various dissociation wavelengths using different bond dissociation energies, we estimate the error in our determination of ΔH_f^0(NCO) to be ±1 kcal/mol.

V. DISCUSSION

The results presented here not only settle the question of the onset of predissociation in the NCO $\widetilde{B}\,^2\Pi$ state, but also explain the observations in previous experiments. In Dixon's original study of the NCO $\widetilde{B}\,^2\Pi \leftarrow \widetilde{X}\,^2\Pi$ system, he attributed the spectral broadening of the (200) ← (000) transition to the onset of predissociation forming N(^2D) +CO products, whereas Crosley[23] interpreted the lower fluorescence lifetime of the $\widetilde{B}\,^2\Pi$ state (100) level relative to the (000) level to mean that the (100) level could dissociate to N(^2D)+CO. Our photodissociation cross section measurements show clearly that *all* vibrational levels of the NCO $\widetilde{B}\,^2\Pi$ state predissociate. The explanation of these seemingly discordant results is given by the photofragment TOF spectra. These show that, in Dixon's and Crosley's experiments, predissociation of the $\widetilde{B}\,^2\Pi$ state was indeed occurring, but it was spin-forbidden dissocia-

tion to N(^4S)+CO products. Their results can therefore be explained if the dissociation rate to these products increases with the level of $\widetilde{B}\,^2\Pi$ state vibrational excitation, causing a noticeable decrease in the fluorescence lifetime for the (100) level and observable broadening in the absorption spectrum for the (200) and higher levels. As mentioned in the Results section, the intensity of the photofragment signal from the (000) level relative to the signal from the higher levels appears to be smaller than in the $\widetilde{B}\,^2\Pi \leftarrow \widetilde{X}\,^2\Pi$ absorption spectrum. This suggests that the dissociation rate from the (000) level is sufficiently slow that the photofragment signal is depleted by spontaneous emission.

The next important issue is the discrepancy between our value for ΔH_f^0(NCO) and the literature value. Our experiment is, in principle, a direct measurement of the N–CO bond dissociation energy, but there are several assumptions in our analysis which must be discussed. The $\widetilde{B}\,^2\Pi \leftarrow \widetilde{X}\,^2\Pi$ transitions in the range of the N(^2D)+CO threshold have not been definitively assigned. In using the photofragment TOF spectra to determine this threshold, we have assumed all the spectroscopic transitions originate from the (000) level of the NCO ground electronic state. This may not be correct, as some of these transitions may be sequence bands originating from vibrationally excited NCO. As discussed in the Analysis section, vibrationally excited NCO can result from photodetachment of vibrationally excited NCO$^-$. However, in the unlikely event that this were somehow the case for all the transitions in Fig. 5, then the true bond dissociation energy would be higher than 2.38 eV and the true ΔH_f^0(NCO) would be lower than 30.5 kcal/mol, a shift in the wrong direction from the literature value. We also assume in our simulations that dissociation occurs in a time which is less than 1% of the total flight time (i.e. <35 ns). This is strongly supported by the observation that the TOF spectra which were taken at both photofragment flight lengths $l=67.8$ and 101.1 cm could be fit with a single fragment translational energy distribution.

Another source of possible error is that our analysis assumes that τ_{min} and τ_{max} in the TOF distributions are from N+CO($v=0$) fragments and, in particular, that the TOF spectra at 255 and 247 nm are due entirely to CO($v=0$). Suppose, however, that no CO($v=0$) is produced at those wavelengths and that the TOF spectra are from N(^2D)+CO($v=1$). If this were the case, D_0(N–CO) would have to be lowered by 5 kcal/mol (corresponding to the CO vibrational frequency) from our value and ΔH_f^0(NCO) would be raised by the same amount, which

would bring it in close agreement with the literature value. However, this would imply that the CO distribution at 241 nm [Fig. 5(e)] is approximately 50% $v=2$, 50% $v=1$, and no $v=0$, a most unusual distribution. In addition, at 261 and 305 nm, where only $N(^4S)+CO$ is formed, the edges of the TOF spectra are reproduced in our simulations using $D_0(N-CO)=2.38$ eV. In order to fit these spectra with a 5 kcal/mol lower bond dissociation energy, one would have to assume no $CO(v=0)$ was produced at these wavelengths, as well. This also seems unlikely, considering the substantial range of CO vibrational states populated at both of these wavelengths, and the different mechanism producing the spin-forbidden product channel. We therefore believe that the bond dissociation energy obtained from our TOF spectra is correct and that the literature value of ΔH_f^0 (NCO) is too large by several kilocalories per mole.

The literature value[26] of ΔH_f^0(NCO) is obtained from three quantities which contain possible sources of error:(1) D^A(H–NCO), the threshold for formation of NCO $\tilde{A}\,^2\Sigma^+$ from the photolysis of HNCO; (2) D_0(HN–CO), the dissociation energy of HNCO to form NH+CO; and (3) ΔH_f^0(NH). The H–NCO bond dissociation energy D_0(H–NCO) is found from D^A(H–NCO) by subtracting 2.82 eV, the electronic energy of the NCO $\tilde{A}\,^2\Sigma^+$ state. We then have

$$\Delta H_f^0(\text{NCO})=D_0(\text{H–NCO})-D_0(\text{HN–CO})+\Delta H_f^0(\text{NH})$$
$$+\Delta H_f^0(\text{CO})-\Delta H_f^0(\text{H}). \qquad (4)$$

The standard heats of formation of CO and H are well known.[44] The literature value of ΔH_f^0(NCO) is based on Okabe's value[22] of 7.73 eV for D^A(H–NCO), Chandler's value[25] of D(HN–CO)$=82.9$ ($+2.8$, -0.7) kcal/mol, which was obtained from the threshold for NH($a\,^1\Delta$) production from HNCO photodissociation, and Berkowitz's value[45] of ΔH_f^0(NH)$=82.5$ kcal/mol, which was obtained from NH$_2$ ionization and dissociative ionization potentials. Two more recent independent measurements[46] of ΔH_f^0(NH) are in excellent agreement with Berkowitz's value. However, a more recent measurement of D^A(H–NCO) by Shobatake[47] yields a slightly lower value 7.65 eV, lowering ΔH_f^0(NCO) by 1.8 kcal/mol. This brings ΔH_f^0(NCO) down from 36.1 to 34.3 kcal/mol. In addition, using the upper bound on D(HN–CO) of 85.7 kcal/mol from Chandler's study lowers ΔH_f^0(NCO) still more (to 31.5 kcal/mol), bringing it within the error bars of our measurement. Our value for ΔH_f^0(NCO) therefore is not as inconsistent with previous work as it might first appear, and a further lowering of D^A(H–NCO) would yield even better agreement.

We also note that Coombe[2] obtained a lower bound to ΔH_f^0(NCO) of 37 kcal/mol in a photodissociation study of NCO at 193 nm based on the highest internal energy seen in the CN fragment. However, his value assumes no internal excitation in the NCO, which is generated by the F +HNCO reaction. The CO bond distances in HNCO and NCO are 1.167 (Ref. 48) and 1.21 Å (Ref. 49), respectively. Based on a simplistic Franck–Condon view of the

F+HNCO reaction, this geometry change would lead one to expect the NCO product to have significant stretching excitation which could, in principle, appear as CN internal excitation when NCO is photodissociated.

Finally, we consider the mechanism for the various NCO dissociation processes. Until very recently, little was known about the detailed structure and interaction of the excited state potential energy surfaces of NCO. Past calculations have been completed at the intermediate neglect of the differential overlap-configuration interaction (INDO-CI)[50] and modified intermediate neglect of differential overlap (MINDO/3)[51] level; predictions of electronic state levels varied widely between these two calculations, with neither being close to the experimentally determined values for the $\tilde{A}\,^2\Sigma^+$ and $\tilde{B}\,^2\Pi$ states. However, a new theoretical study by Alexander and Werner[39] addresses in detail the nature of the potential energy surfaces and the mechanism of the spin-forbidden decomposition of the NCO $\tilde{B}\,^2\Pi$ state using ab initio methods. They propose that the dissociation pathway for this process first passes through a conical intersection between the $\tilde{B}\,^2\Pi$ and $\tilde{A}\,^2\Sigma^+$ states, both of which have components of A' symmetry when the molecule is bent. Dissociation then occurs through the interaction via spin–orbit coupling of the $\tilde{A}\,^2\Sigma^+$ state with the repulsive $^4\Sigma^-$ state which correlates with $N(^4S)+CO$ products. An attractive feature of their calculation is that, for collinear geometries, the minimum in the crossing seam between the $\tilde{B}\,^2\Pi$ and $\tilde{A}\,^2\Sigma^+$ states occurs slightly above the $\tilde{B}\,^2\Pi$ state minimum. This is consistent with the apparent rapid increase in dissociation rate as the vibrational energy of the $\tilde{B}\,^2\Pi$ state increases.

This calculation also predicts that the lowest energy crossing between the $\tilde{A}$ state and the repulsive $^4\Sigma^-$ state occurs at a bond angle of 145.5° and CO bond length of 1.21 Å, which is considerably longer than the bond length of 1.13 Å in diatomic CO. One therefore expects considerable rotational and vibrational excitation of the CO produced by spin-forbidden dissociation of NCO. While we cannot distinguish rotational from vibrational excitation in our TOF spectra of the spin-forbidden channel, the spectra are certainly consistent with extensive excitation of the CO product. Planned experiments with a two-particle position and time sensing detector similar to that used by Los and co-workers[52] should yield more complete product energy distributions, enabling a detailed comparison with theory.

Finally, although Alexander and Werner did not explicitly discuss photodissociation to the spin-allowed products, one can speculate on the possible mechanism based on their results. Neither the $\tilde{A}\,^2\Sigma^+$ nor $\tilde{B}\,^2\Pi$ states correlate to $N(^2D)+CO$ products for linear NCO geometries, but both states correlate to these products for bent geometries. The excited stretching levels of the $\tilde{B}\,^2\Pi$ state that are accessed in our experiment should have some bending character due to Fermi resonances, so dissociation to spin-allowed products should be reasonably facile once this channel becomes energetically accessible. This is consistent with the experimental observation that the spin-allowed channel dominates immediately above the $N(^2D)+CO$ threshold.

VI. CONCLUSIONS

We have used photodissociation spectroscopy to study the $\tilde{B}\,^2\Pi \leftarrow \tilde{X}\,^2\Pi$ electronic transition in NCO. Photodissociation cross section measurements show that predissociation occurs throughout the $\tilde{B}\,^2\Pi$ state, including the ground vibrational level. Time-of-flight spectroscopy of the N+CO photofragments reveal that the first several vibrational levels of the NCO $\tilde{B}\,^2\Pi$ state undergo spin-forbidden dissociation to $N(^4S)+CO$ products, but 20.3 kcal/mol above the $\tilde{B}\,^2\Pi$ state origin, the spin-allowed $N(^2D)+CO$ channel becomes energetically accessible and immediately dominates the photofragment distribution. From our determination of this threshold, we obtain a ΔH_f^0 of 30.5 ± 1 kcal/mol for the NCO free radical, which is significantly lower than the current literature value of 36.1 kcal/mol. We also obtain approximate CO internal energy distributions from the time-of-flight spectrum. The dynamics of NCO photodissociation are discussed briefly in terms of recent theoretical results by Alexander and Werner which indicate that spin-forbidden dissociation from the $\tilde{B}\,^2\Pi$ state occurs via a conical intersection with the $\tilde{A}\,^2\Sigma^+$ state followed by a nonadiabatic transition to a repulsive quartet state which correlates to $N(^4S)+CO$ products.

[1] Molecular Photodissociation Dynamics, edited by M. N. R. Ashfold and J. E. Baggott (Royal Society of Chemistry, London, 1987).

[2] X. Liu and R. D. Coombe, J. Chem. Phys. 91, 7543 (1989).

[3] J. C. Loison, S. H. Kable, P. L. Houston, and I. Burak, J. Chem. Phys. 94, 1796 (1991).

[4] E. J. Hintsa, X. S. Zhao, W. M. Jackson, W. B. Miller, A. M. Wodtke, and Y. T. Lee, J. Phys. Chem. 95, 2799 (1991).

[5] R. E. Continetti, D. R. Cyr, R. B. Metz, and D. M. Neumark, Chem. Phys. Lett. 182, 406 (1991).

[6] B. S. Haynes, Combust. Flame 28, 113 (1977); J. A. Miller, M. C. Branch, W. J. McLean, D. W. Chandler, M. D. Smooke, and R. J. Kee, Symp. Int. Combust. Proc. 12, 673 (1984).

[7] (a) K. N. Wong, W. R. Anderson, A. J. Kotlar, and J. A. Vanderhoff, J. Chem. Phys. 81, 2970 (1984); (b) W. R. Anderson, J. A. Vanderhoff, A. J. Kotlar, M. A. Dewilde, and R. A. Beyer, ibid. 77, 1677 (1982); (c) R. A. Copeland and D. R. Crosley, Can J. Phys. 62, 1488 (1984).

[8] K. Schmatjko and J. Wolfram, Ber. Bunsenges. Phys. Chem. 82, 419 (1978).

[9] R. Holland, D. W. G. Style, R. N. Dixon, and D. A. Ramsay, Nature 182, 337 (1958).

[10] R. N. Dixon, Philos. Trans. R. Soc. London A 252, 165 (1960).

[11] R. N. Dixon, Can. J. Phys. 38, 10 (1960).

[12] E. Milligan and M. E. Jacox, J. Chem. Phys. 47, 5157 (1967).

[13] P. S. H. Bolman, J. M. Brown, A. Carrington, I. Kopp, and D. A. Ramsay, Proc. R. Soc. London, Ser. A 343, 17 (1975).

[14] V. E. Bondybey and J. H. English, J. Chem. Phys. 67, 2868 (1977).

[15] T. R. Charlton, T. Okamura, and B. A. Thrush, Chem. Phys. Lett. 89, 98 (1982).

[16] D. R. Woodward, D. A. Fletcher, and J. M. Brown, Mol. Phys. 62, 517 (1987).

[17] D. Patel-Misra, D. G. Sauder, and P. J. Dagdigian, J. Chem. Phys. 93, 5448 (1990).

[18] A. Carrington, A. R. Fabris, B. J. Howard, and N. J. D. Lucas, Mol. Phys. 20, 961 (1971).

[19] (a) K. Kawaguchi, S. Saito, and E. Hirota, Mol. Phys. 49, 663 (1983); (b) 55, 341 (1985).

[20] (a) C. E. Barnes, J. M. Brown, A. D. Fackerell, and T. J. Sears, J. Mol. Spectrosc. 92, 485 (1982); (b) J. Werner, W. Seebass, M. Koch, R. F. Curl, W. Urban, and J. M. Brown, Mol. Phys. 65, 453 (1985); (c) P. B. Davies and I. H. Davis, ibid. 69, 175 (1990).

[21] (a) D. M. Sonnenfroh, R. G. MacDonald, and K. Liu, J. Chem. Phys. 93, 1478 (1990); (b) D. G. Sauder, D. Patel-Misra, and P. J. Dagdigian, ibid. 95, 1696 (1991); (c) L. F. Phillips, I. A. W. Smith, R. P. Tuckett, and C. J. Whitham, Chem. Phys. Lett. 183, 254 (1991).

[22] H. Okabe, J. Chem. Phys. 53, 5307 (1970).

[23] B. J. Sullivan, G. P. Smith, and D. R. Crosley, Chem. Phys. Lett. 96, 307 (1983).

[24] R. J. Balla and K. H. Casleton, J. Phys. Chem. 95, 2344 (1991), and references therein.

[25] (a) T. A. Spiglanin, R. A. Perry, and D. W. Chandler, J. Phys. Chem. 90, 6184 (1986); (b) T. A. Spiglanin and D. W. Chandler, Chem. Phys. Lett. 141, 428 (1987).

[26] K. -Y. Du and D. W. Setser, Chem. Phys. Lett. 153, 393 (1988).

[27] M. A. Johnson, M. L. Alexander, and W. C. Lineberger, Chem. Phys. Lett. 112, 285 (1984).

[28] R. B. Metz, S. E. Bradforth, and D. M. Neumark, Adv. Chem. Phys. 81, 1 (1992).

[29] D. Proch and T. Trickl, Rev. Sci. Instrum. 60, 713 (1989).

[30] E. Illenberger, P. B. Comita, J. I. Brauman, H. -P. Fenzlaff, M. Heni, N. Heinrich, W. Koch, and G. Frenking, Ber. Bunsenges. Phys. Chem. 89, 1026 (1985).

[31] R. E. Continetti, D. R. Cyr, and D. M. Neumark, Rev. Sci. Instrum. 63, 1840 (1992).

[32] (a) J. M. B. Bakker, J. Phys. E 6, 785 (1973); (b) 7, 364 (1974).

[33] S. E. Bradforth, E. H. Kim, and D. M. Neumark (to be published).

[34] R. N. Dixon, M. J. Trenouth, and C. M. Western, Mol. Phys. 60, 779 (1987).

[35] J. W. C. Johns, Can. J. Phys. 39, 1738 (1961).

[36] (a) D. Gauyacq, C. Larcher, and J. Rostas, Can. J. Phys. 57, 1634 (1979); (b) C. Larcher, D. Gauyacq, and J. Rostas, J. Chim. Phys. 77, 655 (1980).

[37] J. A. Pople, Mol. Phys. 3, 16 (1960).

[38] J. T. Hougen, J. Chem. Phys. 36, 519 (1962); 37, 403 (1962).

[39] M. H. Alexander and H.-J. Werner, J. Chem. Phys. (to be published).

[40] (a) M. A. Johnson, J. Rostas, and R. N. Zare, Chem. Phys. Lett. 92, 225 (1982); (b) M. A. Johnson, R. N. Zare, J. Rostas, and S. Leach, J. Chem. Phys. 80, 2407 (1984).

[41] R. E. Continetti, Ph.D. thesis, University of California, Berkeley, 1989.

[42] T. N. Kitsopoulos, Ph.D. thesis, University of California, Berkeley, 1991.

[43] R. N. Zare, Mol. Photochem. 4, 1 (1972).

[44] M. W. Chase, Jr., C. A. Davies, J. R. Downey, Jr., D. J. Frurip, R. A. McDonald, and A. N. Syverud, JANAF Thermochemical Tables, 3rd ed. (American Chemical Society and American Institute of Physics, New York, 1986).

[45] S. T. Gibson, J. P. Greene, and J. Berkowitz, J. Chem. Phys. 83, 4319 (1985).

[46] K. M. Ervin and P. B. Armentrout, J. Chem. Phys. 86, 2659 (1987); J. W. Sutherland and J. V. Michael, ibid. 88, 830 (1988).

[47] K. Uno, T. Hikida, A. Hiraya, and K. Shobatake, Chem. Phys. Lett. 166, 475 (1990).

[48] K. Yamada, J. Mol. Spectrosc. 79, 323 (1980).

[49] P. Misra, C. W. Mathews, and D. A. Ramsay, J. Mol. Spectrosc. 130, 419 (1988).

[50] P. Carskey, J. Kuhn, and R. Zahradnik, J. Mol. Spectrosc. 55, 120 (1975).

[51] B. F. Minaev, N. M. Ivanova, and Z. M. Muldahmetov, Spectrosc. Lett. 22, 901 (1989).

[52] D. P. de Brujin and J. Los, Rev. Sci. Instrum. 53, 1020 (1982).